nature nanotechnology

LETTERS

PUBLISHED ONLINE: 22 MAY 2011 | DOI: 10.1038/NNANO.2011.68

Spin–orbit-driven ferromagnetic resonance

D. Fang[1], H. Kurebayashi[1], J. Wunderlich[2,3], K. Výborný[2†], L. P. Zârbo[2], R. P. Campion[4], A. Casiraghi[4], B. L. Gallagher[4], T. Jungwirth[2,4] and A. J. Ferguson[1*]

Ferromagnetic resonance is the most widely used technique for characterizing ferromagnetic materials[1]. However, its use is generally restricted to wafer-scale samples or specific micro-magnetic devices, such as spin valves, which have a spatially varying magnetization profile and where ferromagnetic resonance can be induced by an alternating current owing to angular momentum transfer[2–4]. Here we introduce a form of ferromagnetic resonance in which an electric current oscillating at microwave frequencies is used to create an effective magnetic field in the magnetic material being probed, which makes it possible to characterize individual nanoscale samples with uniform magnetization profiles. The technique takes advantage of the microscopic non-collinearity of individual electron spins arising from spin–orbit coupling and bulk or structural inversion asymmetry in the band structure of the sample[5,6]. We characterize lithographically patterned (Ga,Mn)As and (Ga,Mn)(As,P) nanoscale bars, including broadband measurements of resonant damping as a function of frequency, and measurements of anisotropy as a function of bar width and strain. In addition, vector magnetometry on the driving fields reveals contributions with the symmetry of both the Dresselhaus and Rashba spin–orbit interactions.

The principle of the spin–orbit ferromagnetic resonance (SO-FMR) technique is illustrated in Fig. 1a. When an alternating electrical current traverses through the uniformly magnetized material, the resulting non-equilibrium distribution of occupied states in the SO-coupled carrier bands yields a non-equilibrium time-dependent spin polarization[7–10]. The polarization produces a transverse component of the internal exchange field, and a torque is applied that drives the precession of the magnetization vector[11,12]. The SO-induced driving field in uniform magnets has been previously used for magnetization switching in the ferromagnetic semiconductor (Ga,Mn)As[5] and for domain nucleation in a $Pt/Co/AlO_x$ stack[6].

The micro- and nanobars used in our study are patterned from 25-nm-thick films of $(Ga_{0.94},Mn_{0.06})As$ and $(Ga_{0.94},Mn_{0.06})(As_{0.9},P_{0.1})$. To drive the FMR we pass a microwave-frequency current through the nanobar (Fig. 1b). For detection we use a frequency mixing effect based on anisotropic magnetoresistance (AMR)[13–18]. When magnetization precession is driven, there is a time-dependent change $\Delta R(t)$ in longitudinal resistance from the equilibrium value R (owing to AMR). The resistance oscillates with the same frequency as the microwave current, thus causing frequency mixing, and a directly measurable d.c. voltage V_{dc} is generated. This voltage provides a direct probe of the amplitude and phase of magnetization precession with respect to microwave current.

We first present measurements on an 80-nm-wide nanobar patterned in the [1$\bar{1}$0] direction from the (Ga,Mn)(As,P) epilayer. The magnetic field dependence of V_{dc} is measured at different microwave frequencies and taken at a temperature of 6 K. The frequency

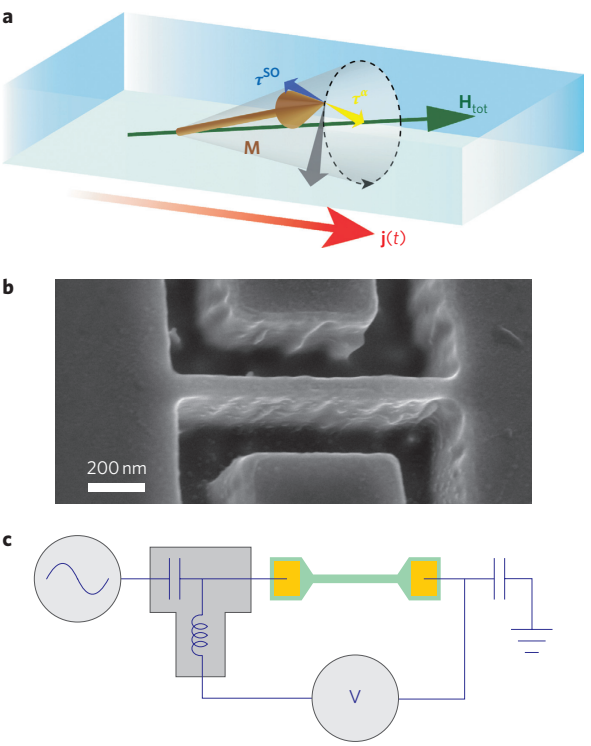

Figure 1 | Principle of the experiment and setup. a, Precession of the magnetization vector **M** around the total magnetic field $\mathbf{H}_{tot}$. **M** is subject to a damping torque τ^{α} (yellow arrow) owing to energy dissipation, which causes the magnetic motion to relax towards $\mathbf{H}_{tot}$. The driving torque τ^{SO} owing to the current-induced effective field counters the effect of damping, and leads to steady-state motion $\partial\mathbf{M}/\partial t = -\gamma\mathbf{M} \times \mathbf{H}_{tot}$ (grey arrow). The current density vector is represented by $\mathbf{j}(t)$. **b**, SEM image of an 80-nm-wide bar, patterned from the (Ga,Mn)(As,P) wafer. **c**, Schematic of the experimental setup. A microwave frequency current is driven across the nanoscale magnetic bar, which is contacted with Cr/Au bondpads. The d.c. voltage, generated by magnetization precession, is extracted through a bias tee (represented by the capacitor and inductor network attached between the signal generator and sample source). The d.c. connection at the drain also provides a microwave ground, represented by a capacitor.

of the incident current is fixed while an external d.c. magnetic field $\mathbf{H}_0$ is swept, and a well-defined resonance peak appears (Fig. 2a). The peak is well fitted by the solution of the Landau–Lifshitz–Gilbert (LLG) equation, which describes the dynamics of precessional motion of the magnetization. The resonance lineshape is a combination of symmetric and antisymmetric Lorentzian functions with amplitudes V_{sym} and V_{asy}, respectively.

[1]Microelectronics Group, Cavendish Laboratory, University of Cambridge, JJ Thomson Avenue, Cambridge CB3 0HE, UK, [2]Institute of Physics ASCR, v.v.i., Cukrovarnická 10, 162 53 Praha 6, Czech Republic, [3]Hitachi Cambridge Laboratory, Cambridge CB3 0HE, UK, [4]School of Physics and Astronomy, University of Nottingham, Nottingham NG7 2RD, UK; †Present address: Department of Physics, State University of New York at Buffalo, Buffalo, New York 14260, USA. *e-mail: ajf1006@cam.ac.uk

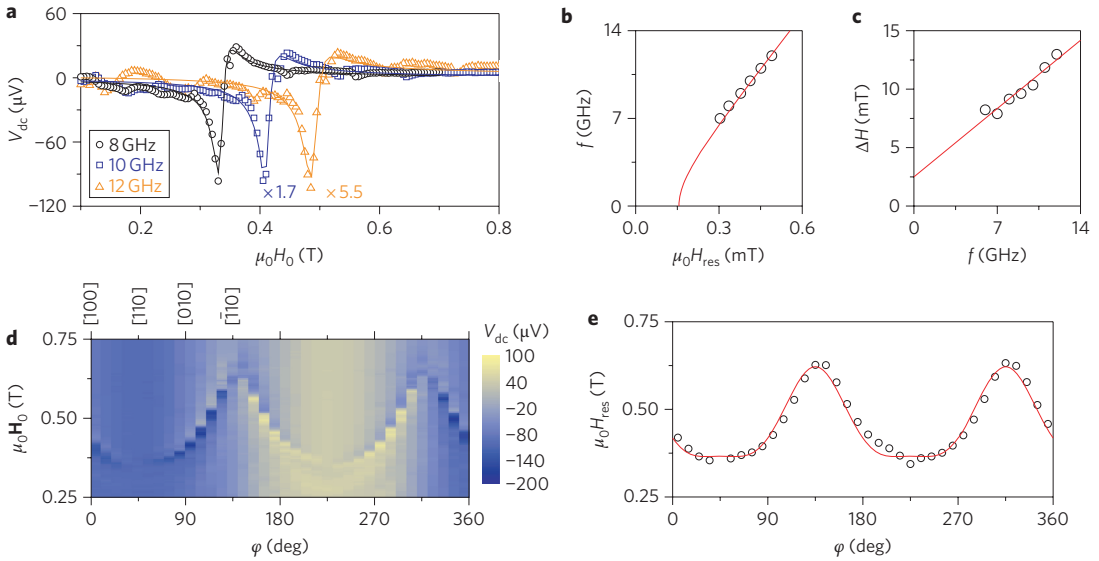

Figure 2 | Spin–orbit-driven ferromagnetic resonance. a, V_{dc} measured at 8, 10 and 12 GHz (symbols) on the 80-nm-wide device. The resonance peaks are clearly observed and can be well described by the solution to the LLG equation (for example equation (32) in ref. 16). Solid lines are the fitted results. The difference in the signal level at different frequencies is caused by the frequency-dependent attenuation of the microwave circuit. **b**, Resonance field H_{res} as a function of microwave frequency. The red solid line is the fitted results to equation (3). **c**, Frequency dependence of the FMR linewidth ΔH. The data are fitted to a straight line to extract ΔH_{inhomo} and α. **d**, V_{dc} measured from in-plane rotational scans of the external field $\mathbf{H}_0$. The colour scale represents the magnitude of the voltage. φ is the angle between the magnetization vector $\mathbf{M}$ and the [100] crystalline axis. **e**, Angle plot of the resonance field H_{res}. The red line is a fitting curve to equations (3) and (4) to calculate the magnetic anisotropy.

Figure 2b plots the frequency dependence of the resonance field H_{res}, which fits well to a modified Kittel formula (see equation (3) in the Methods). The FMR linewidth ($\Delta H = \Delta H_{inhomo} + \alpha\omega/\gamma$) describes the damping in the ferromagnetic system. The broadband nature of the setup allows us to determine the inhomogeneous (2.5 mT) and frequency-dependent contributions to the damping (Fig. 2c) corresponding to a Gilbert damping constant of $\alpha = 0.023$. Using a vector field cryostat, we also performed the SO-FMR measurements for different orientations of the external magnetic field. In Fig. 2d we present the data from an in-plane scan of the magnetic field, showing that there is a strong uniaxial anisotropy perpendicular to the bar direction. By analysing the peak positions (Fig. 2e) using equation (3), we quantify the anisotropy fields and find $\mu_0 H_{2\parallel} = -180$ mT (uniaxial) and $\mu_0 H_{4\parallel} = 68$ mT (biaxial). In addition to the FMR signal, we also note the presence of a non-resonant, angle-dependent background signal (Fig. 2d) owing to a bolometric or thermoelectric effect.

To characterize SO-FMR it is necessary to understand the direction and amplitude of the effective field $\mathbf{h}_{eff}$ that drives magnetization precession. We are able to perform vector magnetometry on the driving field from the angle dependence of the amplitude of the FMR peak[2,3]. For a vector driving field $\mathbf{h}_{eff}(t) = (h_x, h_y, h_z)e^{i\omega t}$ in phase with the microwave current $\mathbf{I}(t) = (I, 0, 0)e^{i\omega t}$, the amplitudes of the two components of the FMR peak are (see Supplementary Information for the derivation)

$$V_{sym}(\theta) = \frac{I\Delta R}{2} A_{sym} \sin(2\theta) h_z \quad (1)$$

$$V_{asy}(\theta) = \frac{I\Delta R}{2} A_{asy} \sin(2\theta)(h_x \sin\theta + h_y \cos\theta) \quad (2)$$

where ΔR is the non-crystalline AMR coefficient of the ferromagnetic sample, θ is the angle between the applied field $\mathbf{H}_0$ and the current $\mathbf{I}$, and $A_{sym(asy)}$ are constants determined by the magnetic anisotropies. Hence, by decomposing the resonance lineshape into V_{sym} and V_{asy}, and by measurements of the AMR and magnetic anisotropies, we are able to deduce the components of $\mathbf{h}_{eff}$. In the Supplementary Information, we verify this vector magnetometry technique in a sample where FMR is driven by the microwave magnetic field from a short-circuited waveguide.

No component of V_{sym} is seen to behave as $\sin(2\theta)$, indicating that the driving field $\mathbf{h}_{eff}$ is predominantly in-plane. Accordingly, we restrict our discussion to V_{asy} (a comparison of V_{asy} and V_{sym} is found in the Supplementary Information). Figure 3a shows the angle dependence of V_{asy} for a 500-nm-wide (Ga,Mn)As bar patterned in the [1$\bar{1}$0] direction. We see that $V_{asy}(\theta)$ comprises a $-\sin(2\theta)\cos(\theta)$ term, indicating that the driving field is perpendicular to $\mathbf{I}$. In a [110] device (Fig. 3a) the amplitude of V_{asy} has opposite sign, indicating that the driving field has reversed. For nanobars along [100] and [010] (Fig. 3b), the V_{asy} curve is a superposition of $\sin(2\theta)\sin(\theta)$ and $\sin(2\theta)\cos(\theta)$ functions, showing that the driving field consists of components both parallel and perpendicular to $\mathbf{I}$.

These data are most clearly seen by plotting the dependence of the magnitude and direction of the effective field on the current (nanobar) orientation (Fig. 3c). Two contributions to the driving field are observed, with different symmetry, $\mathbf{h}_{eff} = \mathbf{h}_D + \mathbf{h}_R$. Quantitative microscopic understanding of these contributions is provided by calculations that are described in detail in the Supplementary Information. The theory links the SO-FMR driving fields to the inversion-symmetry-breaking terms in the relativistic 3D Hamiltonian of the ferromagnetic semiconductor, $\mathcal{H}_{C4} = C_4 \sum_i J_i k_i (e_{i+1\,i+1} - e_{i+2\,i+2}) + C_4 \sum_i (J_i k_{i+1} - J_{i+1} k_i) e_{i\,i+1}$ (refs 5,19). These terms originate from the combined effects of inversion asymmetry of the bulk zinc-blende lattice and uniform strain. Here $\mathbf{J}$ is the hole total angular momentum operator, $\mathbf{k}$ is the wavevector, $\mathbf{e}$ is the strain tensor and $C_4 \approx 0.5$ eV nm for the GaAs semiconductor host. The first term in $\mathcal{H}_{C4}$, which yields $\mathbf{h}_D$, is present in our samples owing to the substrate–ferromagnet lattice matching growth strain, $e_{xx} = e_{yy} \neq e_{zz}$. It depends only on the in-plane (x and y) components of the angular momentum and wavevector and, up to a prefactor, is identical to the Dresselhaus SO Hamiltonian of a 2D electron gas. As expected from the model, our experimental data (Fig. 3c,d) show that $\mathbf{h}_D$

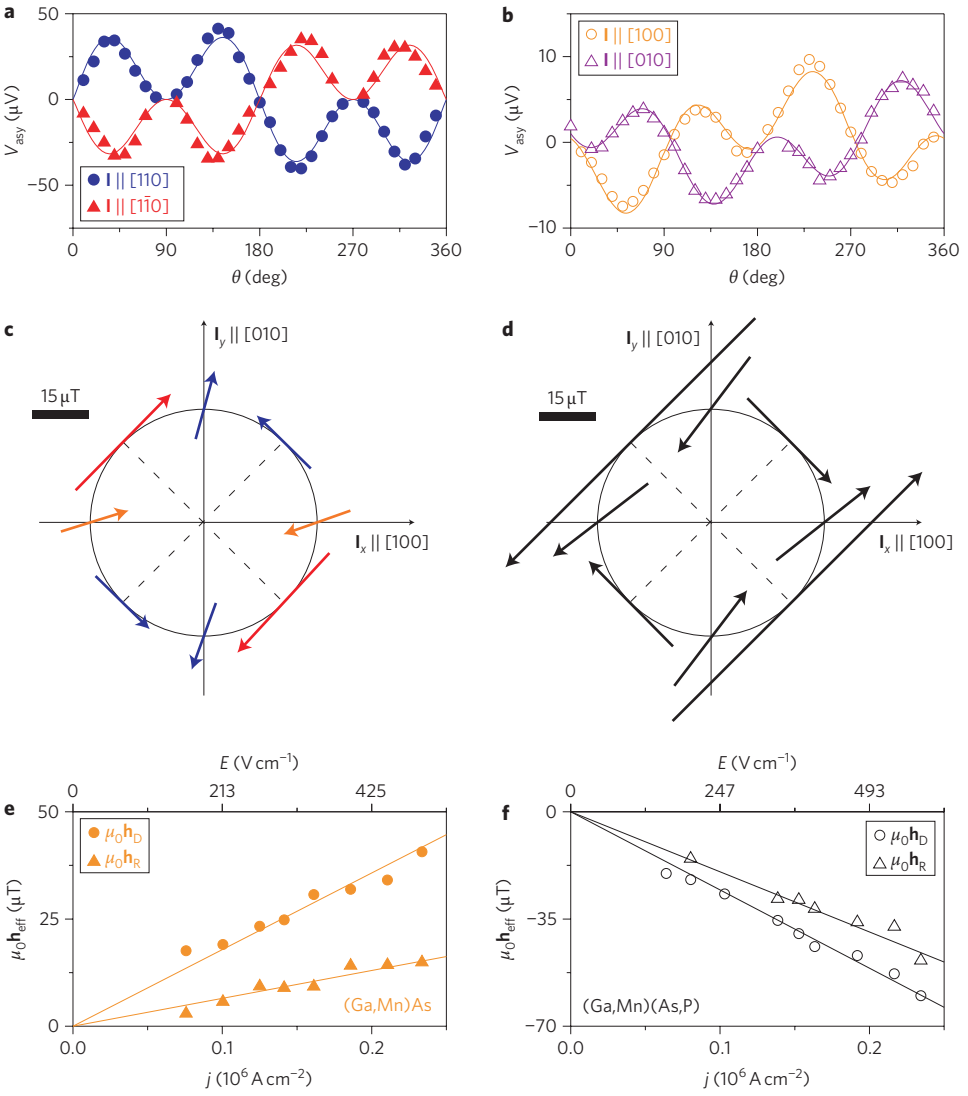

Figure 3 | Characterization of the driving field in both (Ga,Mn)As and (Ga,Mn)(As,P) devices. a,**b**, Amplitudes of the anti-symmetric part of the FMR signal V_{asy}, measured on a group of 500-nm-wide (Ga,Mn)As bars, patterned along different crystalline directions. The solid lines are fitted results to equation (2). **c**, Plot of the magnitude and direction of the current-induced effective field $\mathbf{h}_{eff}$ measured on the (Ga,Mn)As nanobars, scaled for a current density $j = 1 \times 10^5$ A cm^{-2}. **d**, Similar plot for $\mathbf{h}_{eff}$ measured on the (Ga,Mn)(As,P) devices. **e**,**f**, Current density dependence of $\mathbf{h}_D$ and $\mathbf{h}_R$ in both (Ga,Mn)As and (Ga,Mn)(As,P) nanobars. A second horizontal scale is included for the electric field, calculated from the device resistance (values given in Methods).

changes sign as the strain changes from compressive ((Ga,Mn)As) to tensile ((Ga,Mn)(As,P)). The second term in $\mathcal{H}_{C4}$ yields the observed $\mathbf{h}_R$ if it takes a form analogous to the 2D Rashba SO Hamiltonian, that is, if $e_{xy} = e_{yx} \neq 0$. This shear strain is not physically present in the crystal structure of ferromagnetic semiconductor epilayers. It has been introduced, however, in previous studies to model the in-plane uniaxial anisotropy present in (Ga,Mn)As, and the values of this effective off-diagonal strain are typically several times smaller than the diagonal, growth-induced strain[20]. This is consistent with the observed smaller magnitude of $\mathbf{h}_R = 6.5$ μT than $\mathbf{h}_D = 18$ μT (values given at $j = 1 \times 10^5$ A cm^{-2}). Furthermore, $\mathbf{h}_R$ may contain a contribution from the Oersted field (discussed in the Supplementary Information). Both $\mathbf{h}_D$ and $\mathbf{h}_R$ are measured to be linear in current density (Fig. 3e,f). This measurement was performed for bars in the [100] direction, where it is possible to independently resolve contributions to $\mathbf{h}_R$ and $\mathbf{h}_D$. We observe a larger magnitude of $\mathbf{h}_D$ at a given current density in the (Ga,Mn)(As,P) nanobars. This is explained by the larger magnitude of the growth strain and larger resistivity (larger E at given j) of (Ga,Mn)(As,P) as compared with the (Ga,Mn)As film[21].

We now demonstrate that SO-FMR can be applied to comparative investigations of nanobars where the anisotropies differ from bulk values[22–25]. We first compare the effect of strain relaxation between 500 nm bars under compressive ((Ga,Mn)As) and tensile ((Ga,Mn)(As,P)) growth strain. The in-plane anisotropies are studied; although (Ga,Mn)(As,P) is out-of-plane magnetized[21], the applied field $\mathbf{H}_0$ brings the magnetization into plane. In (Ga,Mn)As we observe an additional uniaxial contribution to the anisotropy ($\mu_0 H_U = 32$ mT) along the bar (Fig. 4a,c) with a magnitude similar to previous reports[22,24,25]. In contrast, in the (Ga,Mn)(As,P) nanobar (Fig. 4b,c) the sign of the uniaxial anisotropy ($\mu_0 H_U = -30.5$ mT) has reversed and the easy axis is now perpendicular to the bar. This can be understood in terms of the sign of the strain relaxation: these materials become magnetically easier in the direction of most compressive (least tensile) strain. So when the tensile strain of the (Ga,Mn)(As,P) nanobar relaxes, it introduces an easy axis perpendicular to the bar. Furthermore, we measured (Ga,Mn)(As,P) bars of different widths (Fig. 4e) and observed a decrease in the strain-relaxation-induced anisotropy from the 80 nm bar ($\mu_0 H_U = -270$ mT) to the 500 nm bar

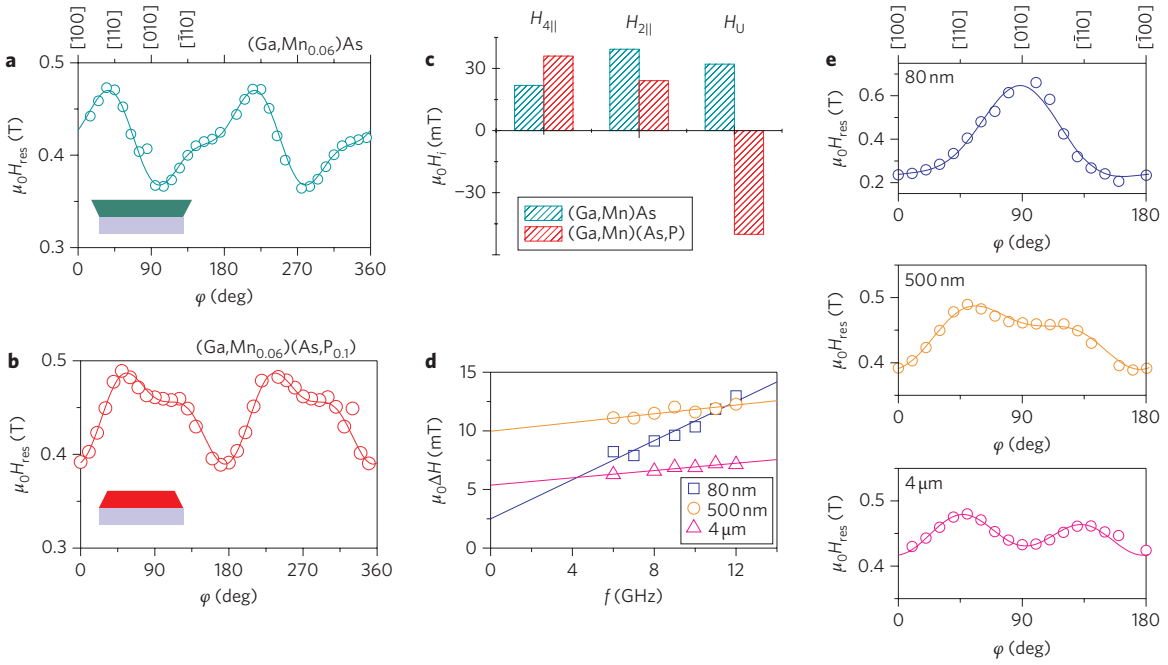

Figure 4 | SO-FMR on devices patterned from different materials and with various sizes. a, $H_{res}(\varphi)$ measured from an in-plane rotational scan on a 500-nm-wide $(Ga,Mn_{0.06})As$ bar (patterned along the [010] axis). The circles are measurement data, and the solid line is the fitted result to equations (3) and (4). **b**, $H_{res}(\varphi)$ measured on a $(Ga,Mn_{0.06})(As,P_{0.1})$ device with identical shape and orientation. **c**, Comparison of the in-plane anisotropy fields H_i between the two samples. **d**, Linewidth ΔH of the FMR signals measured on the 80 nm, 500 nm and 4 μm (Ga,Mn)(As,P) bars. **e**, Comparison of the magnetic anisotropy (in terms of the profiles of H_{res}) of 80 nm, 500 nm and 4 μm (Ga,Mn)(As,P) bars.

($\mu_0 H_U = -30.5$ mT), and almost no effect of strain relaxation in the 4 μm bar ($\mu_0 H_U = -10.5$ mT).

As well as being able to determine the patterning-induced change in anisotropy, we also compare the damping among nanobars of different sizes (Fig. 4d). The frequency-dependent term (related to damping) increases for decreasing bar width: $\alpha = 0.004$ (4 μm wide), 0.006 (500 nm) and 0.023 (80 nm). The significantly higher value of Gilbert damping at 80 nm compared with the 500 nm and 4 μm bars may be owing to damage during the etching process. The frequency-independent term is relevant in the case of strain relaxation because it indicates the inhomogeneity of anisotropy fields within the bar itself. The intermediate case of 500 nm shows greater inhomogeneity, $\Delta H_{inhomo} = 9.9$ mT, than the 4 μm bar, $\Delta H_{inhomo} = 5.4$ mT, explained by the increased variation in local anisotropy. In contrast, the 80 nm bar reduces to $\Delta H_{inhomo} = 2.5$ mT, indicative of a high degree of strain relaxation. The values of α and ΔH_{inhomo} for the 4 μm bar are comparable to measurements on bulk material by conventional FMR[26].

In conclusion, we have performed variable-frequency FMR experiments on individual micro- and nanobars of uniform ferromagnetic semiconductors (Ga,Mn)As and (Ga,Mn)(As,P). FMR is driven by a torque at microwave frequencies, the origin of which lies in the internal effective field (owing to SO coupling and exchange interaction) of the probed ferromagnet. Our work demonstrates a new FMR technique applicable to the magnetic characterization of uniform ferromagnetic nanostructures and to the study of the current-induced effective magnetic fields in SO-coupled ferromagnets.

Methods

Sample preparation. The 25-nm-thick $(Ga_{0.94},Mn_{0.06})As$ and $(Ga_{0.94},Mn_{0.06})(As_{0.9},P_{0.1})$ epilayers were grown by molecular beam epitaxy at 230 °C on semi-insulating GaAs substrates. The (Ga,Mn)As samples were subsequently annealed at 190 °C for 20 h in air, and reached Curie temperature $T_C \approx 130$ K. The (Ga,Mn)(As,P) samples were annealed at 180 °C for 48 h with $T_C \approx 110$ K. The devices were defined on the wafers by 200-nm-wide isolation trenches (~150 nm deep), which were patterned using electron-beam lithography and reactive etching. Cr/Au (20/200 nm) Ohmic contacts were thermally evaporated. Typical longitudinal resistances of 500-nm-wide bars were $R = 17$ kΩ and $R = 20$ kΩ for the $(Ga_{0.94},Mn_{0.06})As$ and $(Ga_{0.94},Mn_{0.06})(As_{0.9},P_{0.1})$ samples, respectively. The contact resistance of $(Ga_{0.94},Mn_{0.06})As$ samples was $2R_c = 1.6$ kΩ, with a similar value expected for $(Ga_{0.94},Mn_{0.06})(As_{0.9},P_{0.1})$.

Measurement technique. The sample was wire-bonded between an open-circuit coplanar transmission line and a low-frequency connection, which also provided a microwave ground. A lock-in technique was used to improve the signal-to-noise ratio in our measurements: the microwave current was pulse modulated and a lock-in amplifier was then referenced to the modulation frequency (987.6 Hz). The difference in d.c. voltage across the sample between the two states, $V = V(I_{on}) - V(I_{off})$, was measured.

Calculating the magnetic anisotropy. The modified Kittel formula, which relates the magnetic anisotropies and the resonance frequency, is given as[27]

$$\left(\frac{\omega}{\gamma}\right)^2 = \mu_0^2 (H_{res} + H'_{ani})(H_{res} + H''_{ani}) \quad (3)$$

where H'_{ani} and H''_{ani} are terms containing the demagnetization and anisotropy energies of the ferromagnet:

$$\begin{aligned} H'_{ani} &= M_s - H_{2\perp} + \frac{H_{4\parallel}}{4}(3 + \cos 4\varphi) + H_{2\parallel}\cos^2\left(\varphi + \frac{\pi}{4}\right) + H_U \sin^2\varphi \\ H''_{ani} &= H_{4\parallel}\cos 4\varphi - H_{2\parallel}\sin 2\varphi - H_U \cos 2\varphi \end{aligned} \quad (4)$$

Here φ is the angle between the magnetization vector **M** and the [100] crystal direction, and M_s is the saturation magnetization. $H_{2\perp}$ is the out-of-plane uniaxial anisotropy ($H_{2\perp} > 0$ for the perpendicular-to-plane easy axis); $H_{4\parallel}$ and $H_{2\parallel}$ represent the in-plane biaxial and uniaxial anisotropy fields, respectively; and H_U models the strain-relaxation-induced uniaxial anisotropy[25] ($H_U > 0$ if its easy axis is along [010]). The anisotropy fields H_i are defined in terms of the anisotropy energy density K_i (units, J cm^{-3}) according to $H_i = 2K_i/\mu_0 M_s$ and conform to the free energy definition in equation (1) of ref. 27.

By fitting the $H_{res}(\varphi)$ data (Figs 2e and 4a,b,e), we were able to determine the in-plane anisotropy fields $H_{4\parallel}$, $H_{2\parallel}$ and H_U in our nano-devices. A gyromagnetic constant γ characteristic for Mn^{2+} spins of 176 GHz T^{-1} (g-factor 2) was used for the fittings.

Note that the above equations are derived for in-plane field scans, with the external field $\mathbf{H}_0$ much larger than M_s, so that $\mathbf{M} \parallel \mathbf{H}_0$. This is the case in our measurements, because the saturation magnetization M_s for (Ga,Mn)As and

(Ga,Mn)(As,P) is typically a few tens of millitesla, whereas the resonance occurs at fields of a few hundred millitesla (for example, see Fig. 2d). The bars are approximated to a uniform magnetized sheet. This is a good approximation for the 500 nm and 4 μm samples, but in the 80-nm-wide bar there is a small contribution to H_U from the in-plane demagnetizing field (calculations shown in Supplementary Information).

Received 28 February 2011; accepted 7 April 2011; published online 22 May 2011

References

1. Vonsovskĭ, S. V. *Ferromagnetic Resonance* (Pergamon, 1966).
2. Tulapurkar, A. A. *et al.* Spin-torque diode effect in magnetic tunnel junctions. *Nature* **438,** 339–342 (2005).
3. Sankey, J. C. *et al.* Spin-transfer-driven ferromagnetic resonance of individual nanomagnets. *Phys. Rev. Lett.* **96,** 227601 (2006).
4. Myers, E. B., Ralph, D. C., Katine, J. A., Louie, R. N. & Buhrman, R. A. Current-induced switching of domains in magnetic multilayer devices. *Science* **285,** 867–870 (1999).
5. Chernyshov, A. *et al.* Evidence for reversible control of magnetization in a ferromagnetic material by means of spin–orbit magnetic field. *Nature Phys.* **5,** 656–659 (2009).
6. Miron, I. M. *et al.* Current-driven spin torque induced by the Rashba effect in a ferromagnetic metal layer. *Nature Mater.* **9,** 230–234 (2010).
7. Aronov, A. G. & Lyanda-Geller, Y. B. Nuclear electric resonance and orientation of carrier spins by an electric field. *JETP Lett.* **50,** 431 (1989).
8. Edelstein, V. Spin polarization of conduction electrons induced by electric current in two-dimensional asymmetric electron systems. *Solid State Commun.* **73,** 233–235 (1990).
9. Inoue, J., Bauer, G. E. W. & Molenkamp, L. W. Diffuse transport and spin accumulation in a Rashba two-dimensional electron gas. *Phys. Rev. B* **67,** 033104 (2003).
10. Silov, A. Y. *et al.* Current-induced spin polarization at a single heterojunction. *Appl. Phys. Lett.* **85,** 5929–5931 (2004).
11. Manchon, A. & Zhang, S. Theory of spin torque due to spin–orbit coupling. *Phys. Rev. B* **79,** 094422 (2009).
12. Garate, I. & MacDonald, A. H. Influence of a transport current on magnetic anisotropy in gyrotropic ferromagnets. *Phys. Rev. B* **88,** 134403 (2009).
13. Costache, M. V., Watts, S. M., Sladkov, M., van der Wal, C. H. & van Wees, B. J. Large cone angle magnetization precession of an individual nanopatterned ferromagnet with dc electrical detection. *Appl. Phys. Lett.* **89,** 232115 (2006).
14. Costache, M. V., Sladkov, M., van der Wal, C. H. & van Wees, B. J. On-chip detection of ferromagnetic resonance of a single submicron Permalloy strip. *Appl. Phys. Lett.* **89,** 192506 (2006).
15. Goennenwein, S. T. B. *et al.* Electrically detected ferromagnetic resonance. *Appl. Phys. Lett.* **90,** 162507 (2007).
16. Mecking, N., Gui, Y. S. & Hu, C-M. Microwave photovoltage and photoresistance effects in ferromagnetic microstrips. *Phys. Rev. B* **76,** 224430 (2007).
17. Hui, X. *et al.* Electric detection of ferromagnetic resonance in single crystal iron film. *Appl. Phys. Lett.* **93,** 232502 (2008).
18. Yamaguchi, A. *et al.* Broadband ferromagnetic resonance of $Ni_{81}Fe_{19}$ wires using a rectifying effect. *Phys. Rev. B* **78,** 104401 (2008).
19. Silver, M., Batty, W., Ghiti, A. & O'Reilly, E. P. Strain-induced valence-subband splitting in III–V semiconductors. *Phys. Rev. B* **46,** 6781 (1992).
20. Zemen, J., Kučera, J., Olejník, K. & Jungwirth, T. Magnetocrystalline anisotropies in (Ga,Mn)As: systematic theoretical study and comparison with experiment. *Phys. Rev. B* **80,** 155203 (2009).
21. Rushforth, A. W. *et al.* Molecular beam epitaxy grown (Ga,Mn)(As,P) with perpendicular to plane magnetic easy axis. *J. Appl. Phys.* **104,** 073908 (2008).
22. Hümpfner, S. *et al.* Lithographic engineering of anisotropies in (Ga,Mn)As. *Appl. Phys. Lett.* **90,** 102102 (2007).
23. Wunderlich, J. *et al.* Local control of magnetocrystalline anisotropy in (Ga,Mn)As microdevices: demonstration in current-induced switching. *Phys. Rev. B* **76,** 054424 (2007).
24. Wenisch, J. *et al.* Control of magnetic anisotropy in (Ga,Mn)As by lithography-induced strain relaxation. *Phys. Rev. Lett.* **99,** 077201 (2007).
25. Hoffmann, F. *et al.* Mapping the magnetic anisotropy in (Ga,Mn)As nanostructures. *Phys. Rev. B* **80,** 054417 (2009).
26. Khazen, K. *et al.* Anisotropic magnetization relaxation in ferromagnetic $Ga_{1-x}Mn_xAs$ thin films. *Phys. Rev. B* **78,** 195210 (2008).
27. Liu, X. & Furdyna, J. K. Ferromagnetic resonance in $Ga_{1-x}Mn_xAs$ dilute magnetic semiconductors. *J. Phys. Condens. Matter.* **18,** R245–R279 (2006).

Acknowledgements

The authors acknowledge fruitful discussions with I. Garate, A. H. MacDonald and L. Rokhinson and support from EU grants FP7-214499 NAMASTE, FP7-215368 SemiSpinNet, ERC Advanced Grant, from Czech Republic grants AV0Z10100521, KAN400100652, LC510, KJB100100802 and Praemium Academiae. D.F. acknowledges support from the Cambridge Overseas Trusts and Hitachi Cambridge Laboratory. A.J.F. acknowledges the support of a Hitachi research fellowship.

Author contributions

D.F. and A.J.F. carried out device fabrication. D.F., H.K., J.W. and A.J.F. conducted experiments and carried out data analysis. K.V., L.P.Z. and T.J. developed the theory. R.P.C., A.C. and B.L.G. provided materials. D.F., A.J.F., T.J., L.P.Z., K.V., H.K. and J.W. all contributed to writing the manuscript. A.J.F. planned the project.

Additional information

The authors declare no competing financial interests. Supplementary information accompanies this paper at www.nature.com/naturenanotechnology. Reprints and permission information is available online at http://www.nature.com/reprints/. Correspondence and requests for materials should be addressed to A.J.F.